Nuclear Inst. and Methods in Physics Research, A 1020 (2021) 165883

Contents lists available at ScienceDirect

Nuclear Inst. and Methods in Physics Research, A

journal homepage: www.elsevier.com/locate/nima

Active neutron interrogation experiments and simulation verification using the SIngle-scintillator Neutron and Gamma-Ray spectrometer (SINGR) for geosciences

L.E. Heffern [a,*], C.J. Hardgrove [a], A. Parsons [b], E.B. Johnson [c], R. Starr [d], G. Stoddard [c], R.E. Blakeley [c], T. Prettyman [e], T.S.J. Gabriel [a,f], H. Barnaby [a], J. Christian [c], M.A. Unzueta [b], C. Tate [g], A. Martin [g], J. Moersch [g]

[a] *Arizona State University School of Earth and Space Exploration, Tempe, AZ, United States of America*
[b] *NASA Goddard Space Flight Center, Greenbelt, MD, United States of America*
[c] *Radiation Monitoring Devices, Watertown, MA, United States of America*
[d] *Catholic University of America, Washington DC, United States of America*
[e] *Planetary Science Institute, Tuscon, AZ, United States of America*
[f] *U.S. Geological Survey, Flagstaff, AZ, United States of America*
[g] *University of Tennessee, Knoxville, TN, United States of America*

ARTICLE INFO

Keywords:
Active interrogation
Geochemical analysis
CLYC
Pulsed neutron generator
Elpasolates
Planetary nuclear spectroscopy

ABSTRACT

We present a new SIngle-scintillator Neutron and Gamma-Ray spectrometer (SINGR) instrument for use with both passive and active measurement techniques. Here we discuss, the application of SINGR for planetary exploration missions; however, hydrology, nuclear non-proliferation, and resource prospecting are all potential areas where the instrument could be applied. SINGR uses an elpasolite scintillator, Cs_2YLiCl_6:Ce (CLYC), that has been shown to have high neutron efficiency even at small volumes, with a gamma-ray energy resolution of approximately 4% full-width-at-half-maximum at 662 keV. Active gamma-ray and neutron (GRNS) measurements were performed with SINGR at the NASA Goddard Space Flight Center (GSFC) Goddard Geophysical and Astronomical Observatory (GGAO) outdoor test site using a pulsed neutron generator (PNG) to interrogate geologically relevant materials (basalt and granite monuments). These experimental results, combined with simulations, demonstrate that SINGR is capable of generating neutron die-away curves that can be used to reconstruct the bulk hydrogen abundance and the depth distribution of hydrogen within the monuments. We compare our experimental results with Monte Carlo N-Particle (MCNP) 6.1 transport simulations to constrain the uncertainties in depth and hydrogen abundance from the neutron die-away data generated by SINGR. For future planetary exploration missions, SINGR provides a single detector system for interrogating the shallow subsurface to characterize the presence and abundance of hydrated phases and to provide bulk elemental analysis.

1. Introduction

1.1. Background

In planetary exploration, neutron spectrometers are commonly used to constrain the hydrogen abundance and depth distribution within the shallow planetary subsurface, while gamma-ray spectrometers are used to quantify the abundance of major and minor elements within rocks and soils. Passive techniques, which use the galactic cosmic ray proton flux as a source of high-energy neutrons within the surface, have historically been used more frequently on planetary missions. However, the Dynamic Albedo of Neutrons (DAN) instrument–which uses two ^{3}He tubes–on the Mars Science Laboratory Curiosity rover has successfully demonstrated active neutron measurements on the surface of Mars. Active neutron data from DAN has identified hydrogen enrichments throughout the traverse and a hidden, buried volcaniclastic, high-silica layer. DAN measurements have also been used to quantify the abundance of hydrated silica phases within fractures and place constraints on specific hydrated amorphous phase abundances [1–4]. The ability of active neutron techniques to support surface planetary exploration missions has been well demonstrated with DAN, and the development of new active neutron interrogation methods is the goal

---

[*] Corresponding author.
E-mail address: lheffern@asu.edu (L.E. Heffern).

https://doi.org/10.1016/j.nima.2021.165883
Received 15 June 2021; Received in revised form 16 September 2021; Accepted 6 October 2021

of several recent and ongoing instrument development programs [4–9]. These development programs use active neutron and gamma-ray measurements to measure the hydrogen content, the depth distribution of hydrogen, as well as the elemental composition of surfaces using a pulsed neutron generator (PNG). The NASA Dragonfly mission to Saturn's moon Titan will also carry an active multiple-detector GRNS instrument (DraGNS) with a neutron generator, these instruments will take surface measurements of Titan while surrounded by the moon's dense, nitrogen-rich atmosphere [9].

Active neutron techniques generally use a neutron source to bombard a sample, then subsequent neutrons and gamma rays emitted by the sample are measured. The incident neutron energy, activation/bombardment duration time, and area materials (including the target, detectors, neutron source, and surrounding environment) determine the returning measured neutron flux and gamma-ray energy spectrum. The number of neutrons and gamma rays produced by these reactions are also proportional to both the concentration of the elements and the incident flux of neutrons [7]. Therefore, a major advantage of active techniques over passive techniques is reduced measurement time due to the significantly higher source particle flux. Typically, active neutron and gamma-ray techniques use a PNG for the neutron source; the emitted PNG neutrons interact in the rocks and soils, become moderated or absorbed, and create characteristic gamma rays. In active neutron spectroscopy a Deuterium Tritium (DT) PNG can be used due to its high energy neutron output via the $^{2}H + {}^{3}H \rightarrow n$ (14.1 MeV) + ^{4}He (3.5 MeV) reaction. PNGs typically pulse at a low frequency to allow the thermal neutrons to leak back out of the surface between each pulse. The magnitude and shape of the neutron arrival in time between each pulse is called "neutron die-away." Neutron die-away experiments bin neutron counts based on their arrival time (time-resolved data) at the detector between each pulse of the PNG. Hydrogen (H), is an efficient neutron moderator; neutron moderators shift the population of fast neutrons towards thermal ($2.5\text{x}10^{-8}$ MeV) energies via scattering interactions. With higher H content, more thermal neutrons are produced. DT neutrons travel at 52,000 km/s, whereas thermal neutrons travel at roughly 2200 m/s, resulting in neutron time-profiles which contain useful information regarding the subsurface distribution of moderators. The H abundance, H distribution with depth, and macroscopic absorption cross section of material surfaces can then be constrained using a neutron die-away curve [10,11]. The shape and magnitude of the neutron die-away curve changes as water-equivalent hydrogen (WEH) increases, this has been explored in previous studies [1,8]. Reconstructing information from a planetary body's subsurface can be accomplished via constraints placed using neutron die-away.

1.2. *Instrument utility*

Here, we describe a new type of active neutron and gamma-ray instrument for planetary exploration missions that uses just a single sensor coupled with a PNG; we directly compare our experimental measurements to MCNP 6.1 transport code results. We demonstrate that the instrument, the SIngle-scintillator Neutron and Gamma-Ray spectrometer (SINGR), is capable of generating time-resolved neutron die-away data and, through simulations, we demonstrate that those data can be used to reconstruct the H content and depth distribution of H within the shallow subsurface (top $\approx$ 15 cm).

SINGR is a single-crystal, Cs_2YLiCl_6:Ce (CLYC), combination neutron and gamma-ray instrument, intended for both passive and active detection. A PNG was used with SINGR to collect neutron die-away data at the NASA Goddard Space Flight Center (GSFC) Geophysical and Astronomical Observatory (GGAO) outdoor gamma-ray and neutron instrumentation testing facility. SINGR is capable of detecting and discriminating both neutrons and gamma rays based on differences in the shape of the scintillator light pulse, allowing for segregation using pulse shape discrimination (PSD) in post-data collection [12,13]. Previous related studies using high-purity germanium (HPGe) gamma-ray detectors at the GSFC GGAO were done to study gamma-ray spectra in gated time windows [5–7,14,15]. CLYC crystals have been used in balloon flight passive measurements [16] and have been implemented for space flight passive measurements [17,18]. In this paper, we report on successful demonstration and simulation verification of active neutron measurements with SINGR, using the die-away technique for geoscience applications.

Active nuclear technologies have been in use for decades in nuclear non-proliferation and safeguards, as well as geologic applications in hydrogeology, hydrology, agriculture, environmental science, and mining [19–21]. CYLC crystals are in use for commercial devices such as the RIIDEye from ThermoFisher Scientific [22]. Current Earth applications of CLYC help to facilitate raising the technological readiness level of SINGR and other space sciences detectors; handheld nuclear instruments have a strong heritage of being successfully adapted to planetary science applications, e.g., the GRNS on the NASA Lunar Prospector mission consisted of commercially available ^{3}He tubes and a standard NaI scintillator [23]; the NASA Psyche mission will also carry similar ^{3}He tubes and a new GRS that shares development with The Detective X handheld from AMETEK ORTEC [24,25].

The recent development of compact PNGs for use in landed planetary science missions has allowed for more possible uses in a variety of different mission scenarios [6,9,11]. This work both improves upon previous studies in the field and presents on the response limitations of a new instrument. SINGR has undergone initial experimental characterization with a PNG at the NASA GSFC GGAO outdoor gamma-ray and neutron instrumentation testing facility. In this paper, we will present on neutron die-away results and model comparisons using SINGR.

2. Experimental setup

2.1. *The SINGR instrument package*

SINGR uses the ultrabright elpasolite scintillator called CLYC which has a dominant $^{6}Li(n, \alpha)t$ reaction, allowing for the detection of neutrons [12,13]. The signal generated by the alpha particle (α) and triton (t) produces a light pulse with a transient response different from that of gamma-ray reactions in CLYC ($\approx$3.2 MeV full energy gamma-ray equivalent energy, GEE). SINGR was tested using a Radiation Monitoring Devices Inc. (RMD) 2-inch diameter by 2-inch long cylindrical CLYC crystal (2" CLYC), coupled to a R6233-100 Hamamatsu photomultiplier tube (PMT) that has been custom modified with an active voltage divider network designed for high count rates. Typical crystal properties of CLYC are shown in Table 1. The data acquisition system (DAQ) used for all experiments is a field-programmable gate array (FPGA) developed by RMD which has a sampling rate of $\approx$250 megasamples per second; Fig. 1 shows the SINGR detector and the FPGA DAQ in its aluminum housing. The mass of SINGR's CLYC sensor head and PMT is approximately 850 grams, the total instrument including detector, DAQ, and housing is less than 3.5 kilograms. The total volume of the detector, DAQ, and housing is approximately 0.05 m^3.

A commercial ThermoFisher MF Physics Model MP320 DT neutron generator with an approximate mass of 12 kg was used for these experiments [30]. This neutron generator is capable of operating as a PNG and can produce up to 10^8 neutrons per second with a limited frequency range from 250 to 1000 Hz (50–200 μs length pulses). Our experiments used a frequency of 250 Hz, which corresponds to a pulse width of 200 μs; we ran the PNG with a current of 60 μA, voltage of 60 kV, and duty factor of 5%, resulting in 2.08×10^7 neutrons per second in 4π. A transistor–transistor logic (TTL) signal (6V pulse ignition, 0V pulse off, 4V during pulse) outputs from the PNG via a BNC output, which is connected to the SINGR FPGA DAQ. For comparison, the PNG onboard MSL has a mass of 2.6 kg and operates with a higher frequency range with an approximate pulse length of 2 μs [10]; future PNGs may be capable of larger frequency ranges [9]. The pulse width of

Table 1
Basic SINGR Cs_2YLiCl_6:Ce (CLYC) crystal material properties are from [12,13,26]. Note that CLYC has three decay constants/times corresponding to the possible allowed energy transition states within the crystal. The efficiency and resolution data were measured during our experiments. The intrinsic pulsed neutron efficiency data (based on PSD value, not GEE peak) was calculated as the total number of measured neutrons of all energies hitting the detector face, divided by the total expected number of neutrons that should be hitting the detector face via MCNP 6.1 simulation. The value in parentheses* denotes the efficiency in the thermal neutron return region only (200–2550 μs). Note that efficiency can change based on the count rate [27]; our pulsed efficiencies are based on the PNG settings described in Section 2.1. The non-pulsed neutron efficiency was determined using a spontaneous fission source (AmBe) at a distance of 1.5 meters and includes all neutron energies. The gamma-ray efficiency and resolution was determined using ^{137}Cs at 15 inches (cm) and calculated to include attenuation in air and aluminum. Uncertainties are based on Poisson statistics and distance, however these uncertainties may be higher for neutrons due to environmental interactions for non-pulsed efficiency values. Similar, non-pulsed efficiency values can be found in [13,28]; the efficiency discrepancy between all neutron energies and thermal region only neutron energies is likely due to the overlap of fast neutrons generated in the ^{35}Cl(n,p)^{35}S reaction in CLYC [29].

Specifications of Cs_2YLiCl_6:Ce	
Density	3.31 g/cm3
2” CLYC crystal mass	341 g
Radiation length	3.42 cm
Melting point	640 °C
Scintillation light yield	20,000 ph/MeV
Peak scintillation wavelength	370 nm
Decay constants	1 ns, 50 ns, 1 μs
Decay time	≈400 ns, 1 μs, 6 μs
GEE for thermal neutrons	3.2 MeV
Specifications of SINGR (2” CLYC)	
SINGR + DAQ mass	<3.5 kg
Thermofisher PNG mass	≈12 kg
DAN PNG mass	≈2.6 kg
Pulsed intrinsic neutron efficiency	20.78 ± 0.02% (9.42 ± 0.02%)*
Intrinsic neutron efficiency (AmBe)	35.5 ± 0.4%
Intrinsic gamma-ray peak efficiency (at 662 keV)	25.8 ± 0.2%
Energy resolution (at 662 keV)	4%

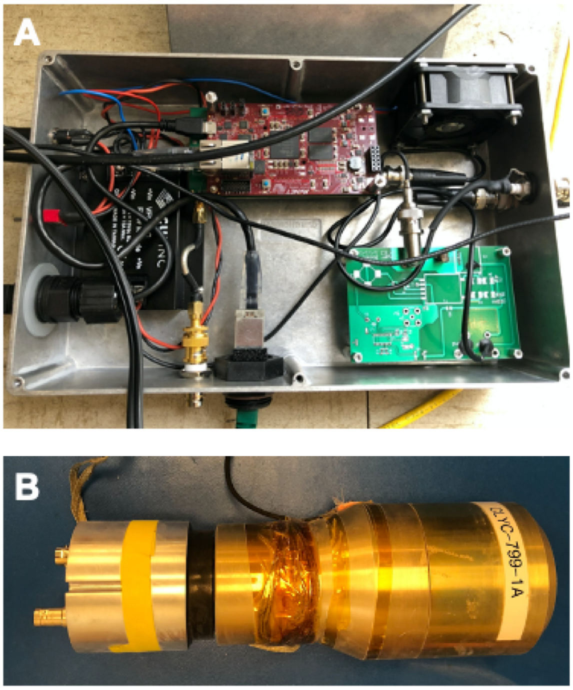

Fig. 1. Prototype SINGR instrument package: (A) RMD data acquisition box with FPGA (≈250 Ms/s) and high-voltage power supply (up to 5 kV via 75 VDC, 15 mA), (B) 2-inch crystal CLYC detector.

the neutron generator affects the magnitude of the neutron count signal seen by SINGR. Ideally, the neutron pulse is short enough that it does not interfere substantially with the relatively low characteristic thermal neutron signal leaking out of the subsurface after moderating interactions. Following previous active measurement studies done by [5,14], we used a 200 μs pulse for studying both neutron and gamma-ray responses in SINGR.

SINGR can be operated at room temperature, so its power consumption is comparable to other scintillators such as NaI, $CeBr_3$, or $LaBr_3$:Ce [31]. However compared to other scintillators, SINGR has a long light-decay time (≈0.4–6 μs), meaning that the signal collection of the detector is relatively slow [26]. This can be an issue in high-event rate environments, unless the efficiency of the detector is well known via strict calibration testing and source monitoring. The proportional response of CLYC provides a typical gamma-ray energy resolution of 4% full-width-at-half-maximum (FWHM) at 662 keV; this is a better energy resolution compared to NaI, 7%–9% FWHM, despite the emission of fewer photons. The neutron absorption cross section of the ^{6}Li in CLYC is more than 2 times that of ^{3}He (at 10 atmospheres), as compared on a volume basis, making it an excellent option for neutron detection [12,13].

2.2. Outdoor instrument test site

SINGR's capabilities have been tested at the NASA GSFC GGAO outdoor gamma-ray and neutron instrumentation testing facility, located a few miles northwest of the Goddard main campus. The test facility houses two large (1.8- x 1.8- x 0.9 m) rock monuments, one made of Concord Granite and the other made of Columbia River Basalt (hereafter referred to simply as granite and basalt, respectively). The PNG and SINGR instruments were operated from a distance via underground power and communications access. The granite monument has ≈0.087 wt% H compared to ≈0.05 wt% H in basalt; the macroscopic thermal neutron absorption cross sections (Σ_a) of the two monuments are Σ_a = 0.01785 cm^{-1} (0.00664 cm^2/g) for basalt and Σ_a = 0.01138 cm^{-1} (0.00433 cm^2/g) for granite, both of which were calculated from an independent elemental assay of the basalt and granite materials (more detailed information, including composition information about the test site, can be found in papers by Bodnarick et al. [5,32]). Active

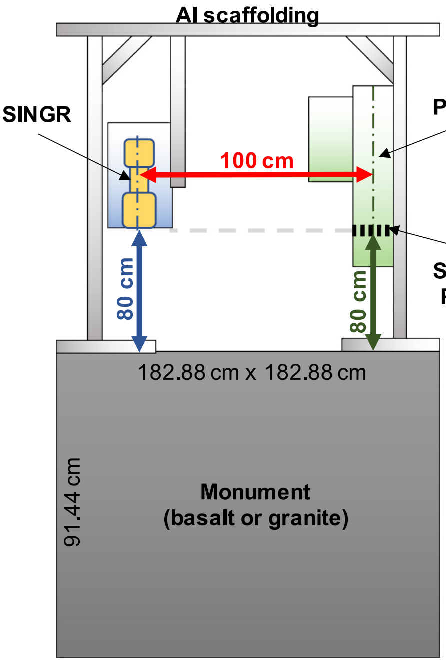

Fig. 2. Geometry diagram for experiments performed using SINGR at GSFC. The aluminum scaffolding (1" extruded light gray boxes) sits on top of the monument material (182.88- x 182.88- x 91.44 cm dark gray box). The SINGR detector (gold object in blue box) is nested inside an aluminum box which is then mounted to the scaffolding via an extruded aluminum arm. The PNG (green) is mounted opposite the SINGR detector to the other side of the scaffolding. The SINGR detector is concentrically distanced from the PNG by 100 cm and its front detection face is level with the PNG source plane at 80 cm from the top of the monument. (For interpretation of the references to color in this figure legend, the reader is referred to the web version of this article.)

measurements with SINGR were performed on both the basalt and granite monuments to demonstrate differences in neutron responses from different target compositions.

The SINGR instrument, electronics, and PNG were mounted onto a 1" x 1" profile extruded aluminum scaffolding that can be moved to sit on top of either the basalt or granite monument. The scaffolding allows for SINGR and the PNG to be adjusted to various heights and relative horizontal distances above the monument. Experiments were performed using the scaffolding, PNG, and detector geometries shown in Fig. 2.

Six different 24" wide x 24" long x 2" thick high-density polyethylene (HDPE) tile configurations were used (Fig. 3) to simulate an increase in wt% H abundance; this included one buried HDPE tile configuration to demonstrate H distribution with depth. Active measurements of both the "Bare" and "HDPE top layer" configurations were taken for both basalt and granite monuments; active measurements of all remaining configurations were only performed on the basalt monument. The buried HDPE tile configuration was tested only within the basalt monument at a depth of 6 inches (15.2 cm). The HDPE tiles contain approximately 14 wt% H and 85 wt% C [33]; when added to a monument, they increase the total wt % H in the topmost layer of the monument. Table 2 shows the approximate calculation for wt % H and WEH in the basalt monument with the HDPE tile configurations. It is important to note that when significantly high amounts of H are present in the top ≈ 15 cm, the neutron sensing depth (neutron number density as a function of depth) will not extend far past the high-H material according to [34], such that the sensing depth of SINGR does not extend to the base of the monument. Note also that SINGR and the PNG are positioned on opposite ends of the monument (Fig. 2) such that SINGR's field of view (FOV) may not encompass the monument's entire top surface.

2.3. Computer modeling of test site

The monument test site is modeled using MCNP 6.1 [35] (Fig. 4) on the Arizona State University *Agave* research computing cluster. The simulation includes the monument (interchangeable as basalt or granite), a simple representation of the aluminum scaffolding on top of the monument, the surrounding atmosphere, an approximation of the ground surrounding the monument, and the SINGR instrument suite. The PNG is fully modeled to include the outer housing and inner materials. The DT reaction within the PNG is modeled as a point source at the approximate location of the source plane within the PNG. The SINGR detector is modeled as a bare 2" tall x 2" diameter cylinder made of CLYC material (not including the surrounding aluminum housing or surrounding mounting box), which uses a ^{6}Li-neutron reaction neutron tally. HDPE tiles and basalt or granite block layers can be added into the monument as needed depending on the desired simulation. All base material cards used in our simulations are based on information provided in Bodnarick et al. 2013 [32]; the weight fraction of H within the base materials (e.g. basalt, granite) is varied and then manually re-normalized using the same methods as Gabriel et al. 2018 [3]. MCNP 6.1 simulations are run using 3×10^{10} NPS (number of particle histories), which is sufficient for producing accurate tally statistics in our configuration [36].

3. Data processing

Measurements taken at the GSFC GGAO basalt and granite monuments resulted in the collection of temporal neutron and gamma-ray data using SINGR. The data sets require significant reduction post factum to separate the neutron signal from the gamma-ray signal using

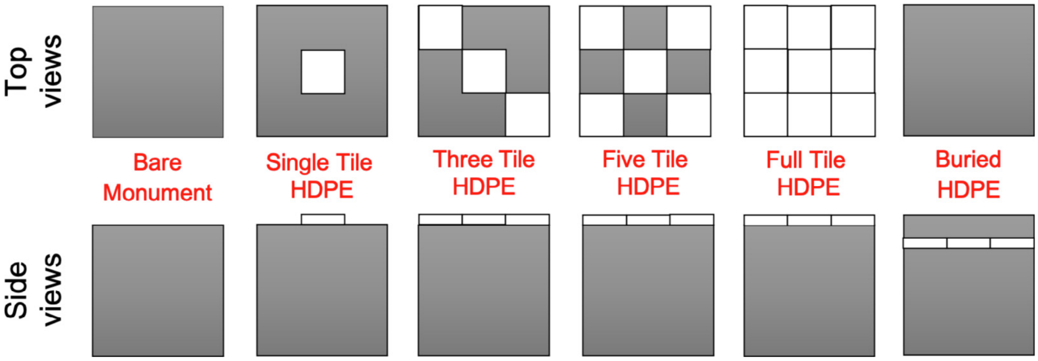

Fig. 3. The six different top layer high-density polyethylene (HDPE) tile configurations used for the basalt and granite monuments and the buried configuration used in the basalt monument. The small, white squares represent HDPE whereas the large, gray squares represent the underlying monument material. The full tile layer of HDPE in the buried configuration can be buried under layers of basalt plates to achieve a variety of burial depths.

Table 2
Calculated H abundances for the HDPE configurations on top of the basalt monument (density of 2.69 g/cc) based on volume, elemental abundance, and density of materials. WEH values are noted in parentheses. The H contribution from HDPE (density of 9.4 g/cc) is calculated using 14 wt% H and 85 wt% C.

Monument configuration	*Wt%H (WEH) Bare*	*Wt%H (WEH) Single tile*	*Wt%H (WEH) Three tiles*	*Wt%H (WEH) Five tiles*	*Wt%H (WEH) Full tiles*
Whole monument	0.050 (0.447)	0.053 (0.475)	0.059 (0.530)	0.065 (0.586)	0.077 (0.697)
Top 15 cm	0.050 (0.447)	0.236 (2.120)	0.593 (5.338)	0.933 (8.398)	1.565 (14.086)

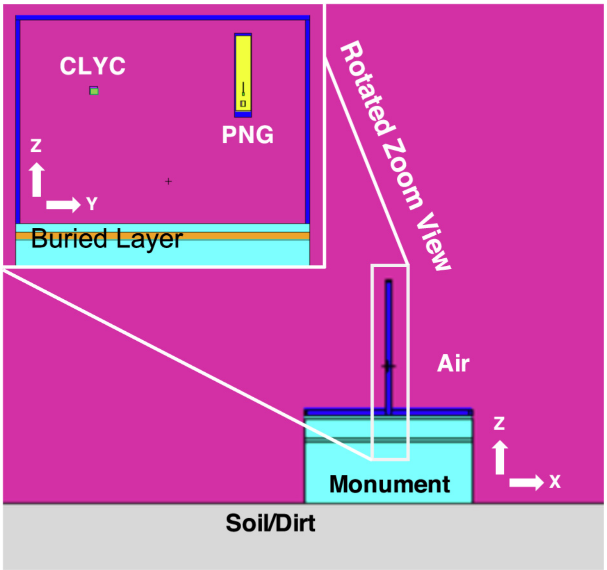

Fig. 4. MCNP 6.1 simulation geometry of the experimental test site with rotated view inset to show buried polyethylene and instrument package; most materials are color coded (pink = air, cyan = basalt or granite monument, blue = aluminum alloy, orange = polyethylene), with gray which represents the soil material as well as the PNG and CLYC instrument package. (For interpretation of the references to color in this figure legend, the reader is referred to the web version of this article.)

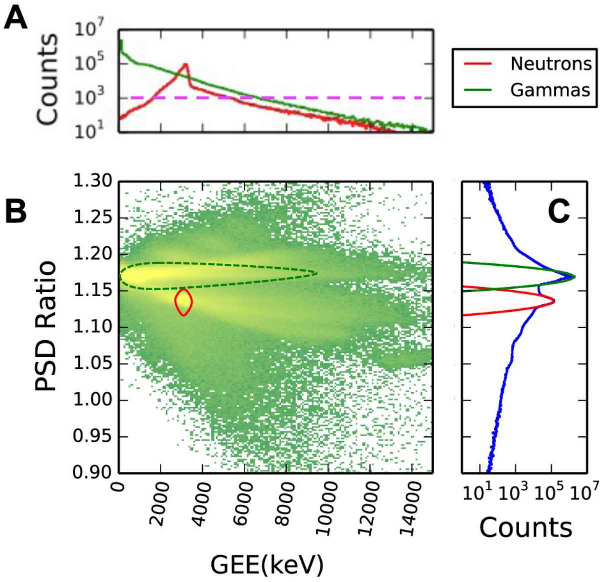

Fig. 5. Pulse shape discrimination (PSD) plots for the SINGR 2-inch CLYC detector using all data from the detector, including during-pulse events, for a typical two-hour measurement on basalt. (A) Counts versus full energy gamma-ray equivalent energy (GEE) of SINGR data for neutrons (red) and gamma rays (green), with horizontal purple line distinguishing total counts above 1000 (greater than 95% confidence in detecting a peak [43]); (B) PSD ratio versus gamma-equivalent energy color mapped for total number of counts on a log scale, the outlines show the *approximate* locations for neutrons (dotted red, lower outline) and gamma rays (dotted green, upper outline) based on a 1000 count threshold; (C) PSD ratio versus count data including two Gaussian fits to neutrons (red, lower) and gamma rays (green, upper). Data shown are from an experiment with the basalt monument at GSFC using a 200 μs pulse PNG. Note that much of the counts outside the red outline for the neutron fit are likely due to fast neutrons [26]. (For interpretation of the references to color in this figure legend, the reader is referred to the web version of this article.)

pulse shape discrimination. Python 2.7 with various SciPy packages was used to discriminate (PSD), interpret, and visualize all data sets [37–40]. Note that on board data processing can be done for flight electronics, as seen on the CLYC-based spectrometer for the NASA LunaH-Map mission [17].

3.1. Pulse-shape discrimination

SINGR uses PSD to identify neutrons and gamma rays based on differences in the shape of the scintillator light pulse. The waveform of the output pulse from the detector is segmented into short (I_s), long (I_L, total in 6 μs), and baseline integrals. I_s and I_L are average baseline integral (B_{avg}) adjusted (the integral divided by the number of samples in the baseline integral) post factum, and then used to determine a pulse shape discrimination ratio. Eq. (1) describes the calculation of the PSD value used to analyze the SINGR data sets:

$$PSD = \frac{I_s - 73 * B_{avg}}{(I_L - 169 * B_{avg}) - (I_s - 73 * B_{avg})}. \tag{1}$$

Note that the values 73 and 169 are the number of samples at 4 ns per sample for the short and long integrals, respectively. Our data sets typically have a neutron PSD ratio ranging from 1.13 to 1.15, whereas gamma rays tend to have a PSD ratio ranging from 1.15 to 1.19. These values appear slightly distorted in Fig. 5 due to high event rates occurring from a disproportionate amount of fast neutron events during the pulse. The fast neutron efficiency in CLYC (occurring from neutron reactions with Cl) is on the order of 1%–2%, these neutrons span in energy from 0–10 MeVee (electron-equivalent energy), which encompasses the thermal neutron peak [41]. The thermal neutron and gamma-ray PSD distributions for CLYC are distinguished from one another based on a figure of merit value [42]. More detailed explanations of interactions in CLYC can be found in [12,13,17,29].

Two Gaussian functions are mapped to the PSD data sets within specified constraints (total PSD ranging 0.5 to 1.5, gamma PSD > 1.15, and 1.11 < neutron PSD < 1.16) using the Python scipy.optimize package [38]; an example of our PSD fit to data is shown in Fig. 5C, along with energy information in Fig. 5A. The data are sorted based on the two PSD sets of Gaussian fit parameters to create two new sub-data sets for neutron flux and gamma-ray flux. A combination of the energy, PSD, and total count data is shown in Fig. 5B. All sub-data sets have their original event-by-event data information preserved, such as a timestamp, full integral (related to particle energy), long integral, short integral, TTL signal (PNG pulse status), and event number. We do not constrain on full integral (energy) events when computing the PSD; as such, fast neutron events are present in our results.

3.2. Neutron data processing

SINGR neutron flux data are divided into 64 lognormal time bins, adhering to the same methods used by the DAN science team to help provide a direct comparison of our instrument package to a known planetary experiment [10,11]. In a single two-hour data set, there can be up to 10^7 total events in the detector. Using the TTL signal from the PNG, each 0–2400 μs PNG period (pulse on and pulse off duration) can be co-added based on the TTL signal (i.e. 6V ignition) to produce a smooth neutron response profile, i.e., a *neutron die-away curve*.

Count rates shown in the results section of this paper are normalized to the sum of the output pulse of the PNG (termed *pulse region normalized*); this is done to account for any variability in total time between measurements. Uncertainty in observed count rate ($\sigma_{observed}$) is propagated for each time bin and is determined based on Poisson statistics ($\sqrt{N_{observed}} = \sigma_{observed}$), assuming the accumulated counts ($N_{observed}$) are Poisson random variates [19].

In this paper, we compare both pulse-region normalized and *thermal region normalized* neutron die-away curves to examine die-away profile shape changes, which can indicate a difference in bulk neutron cross section. The thermal region normalized method of constructing neutron die-away curves is actively used by members of the MSL DAN science team [2,3]. The pulse-region normalized methods are similar to that of Mitrofanov et al. 2014 and Sanin et al. 2015 [44,45]; however in our case, we do not include correction factors to account for the rover body. To pulse region normalize a 200 μs pulse, we normalize over the leading end of the pulse region from 0 to 76 μs, which corresponds to time bins from 0 to 10.

Comparisons between experimental and MCNP simulated neutron die-away curves are done using the same methods outlined in the supplement of Gabriel et al. 2018 [3]. However, here, we perform a simple reduced chi-squared (χ^2/m) analysis using the following equation:

$$\frac{\chi^2}{m} = \sqrt{\sum_{Bin_0}^{Bin_f} \frac{N^2_{observed} - N^2_{expected}}{\sigma^2_{observed} + \sigma^2_{expected}}}, \tag{2}$$

where m is the total number of time bins, $N_{observed}$ is the observed number of normalized counts in a single time bin with normalized uncertainty $\sigma_{observed}$, $N_{expected}$ is the MCNP/simulated output number of normalized counts in the same time bin with normalized uncertainty $\sigma_{expected}$ (based on MCNP relative error), and Bin_0 and Bin_f are the starting time and ending time bins to be compared. Relative errors across our simulations are $< 0.02\%$.

Based on simple neutron time-of-flight calculations, we determined that end-point inclusive time bins 22 through 44 (240–1180 μs) best represent the bins in which the majority of thermal neutrons are returning to the detector from within the monument (Bin_0 and Bin_f, respectively); these are the bins used for thermal region normalization. Additional thermals arriving to the detector from 200–240 μs are likely back scattered inside the mechanical structures close to the detectors and/or the neutron generator. Thermal neutrons arriving after 1180 μs are still returning from deep within the target monument but are statistically insignificant compared to additional counts that may be returning from the nearby ground around the monument, objects outside of the monument (piles of basalt bricks, instrument cases, etc. often placed at random), or due to natural background. In our experimental analyses, we did not include background subtraction; in our simulations we did not include small objects placed outside the monument.

4. Neutron die-away results

Neutron die-away curves were constructed from SINGR experimental data for all configurations from Fig. 3 using the basalt monument and for the bare and full tile HDPE configurations using the granite monument. All data shown in the results section are pulse region normalized. The integrated thermal neutron albedos (total raw counts from 200–2250 μs) for all experiments are shown in Table 3.

4.1. Polyethylene top layer configurations

Neutron die-away experiments were performed on the basalt monument for the bare configuration, as well as top layer HDPE configurations listed from Fig. 3; the results of these experiments are shown in Fig. 6. As the number of HDPE tiles increases, the total neutron count rate in time bins from 200–2250 μs (thermal neutron return region) increases in magnitude; this corresponds to the increase in H abundance.

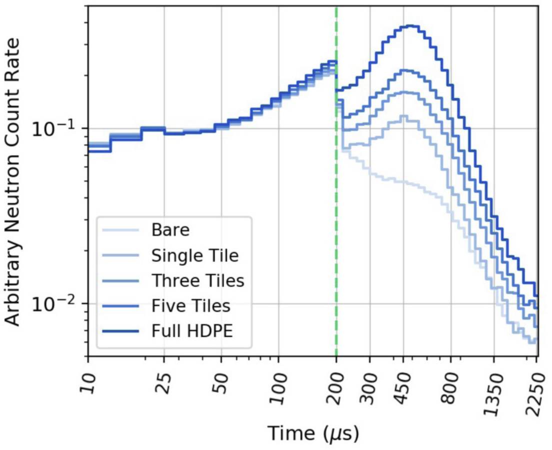

Fig. 6. Polyethylene configuration experimental neutron die-away results. As more HDPE tiles are added, the total wt% H in the FOV of the SINGR instrument suite increases. The total neutron count rate in the thermal neutron region (time bins 200–2250 μs) changes for each configuration, increasing in magnitude as H increases. The green dotted line represents the end of the PNG pulse (≈ 200 μs). The maximum number of thermal neutrons returning to the detector occurs at ≈ 470 μs for the full HDPE tile configuration. (For interpretation of the references to color in this figure legend, the reader is referred to the web version of this article.)

4.2. Buried polyethylene

Fig. 7 shows the neutron die-away curves for a layer of HDPE tiles (2" thick) buried under 6" of basalt, versus the bare basalt, and the full HDPE tile basalt monument configurations. The basalt in the monument is ≈0.05 wt% H based on the elemental assay reported by Bodnarick 2013 et al. [5]. The maximum count rate of neutrons in the thermal region of the die-away curve for the full HDPE tile configuration occurs at ≈ 470 μs. The buried HDPE neutron die-away curve has both a lower overall count rate in the thermal neutron region, and the maximum neutron count rate for returning neutrons occurs in later time bins (≈ 620 μs) compared to the unburied HDPE. Neutrons have a longer distance to travel within the 6" of basalt, which increases the return time to the detector. The buried HDPE die-away curve is also higher in neutron count rate magnitude for the thermal region compared to the bare monument due to the buried H-rich HDPE tile layer.

4.3. Basalt vs. Granite monument

Experiments of bare and full HDPE top tile were performed on both the basalt and granite monuments. The results of these experiments can be seen in Fig. 8. The die-away curve for the full HDPE top tile configurations (high-H) are indistinguishable between basalt and granite, whereas the shape of the die-away curve is different between the bare monuments (low-H). The total macroscopic thermal neutron absorption cross sections for basalt and granite have a percent difference of around 44%.

4.4. Pulse stability

The pulse variability of the PNG used in these studies (refurbished and calibrated in Fall 2018) was estimated using SINGR to measure the total neutron counts during the pulse. Two bare monument configuration data sets from two different dates (7/16/19, 7/24/19 with aluminum scaffolding raised by 6") were investigated, as well as a

Table 3
GGAO active test configurations, total number of returning neutrons (200–2250 μs) per total pulse registered in SINGR using a DT (14.1 MeV neutrons) PNG with a 200 μs pulse width (10^7 nps).

Target	*Bare*	*HDPE single tile*	*HDPE three tiles*	*HDPE five tiles*	*HDPE full tiles*
Basalt	1.14 ± 0.02	1.86 ± 0.05	2.67 ± 0.05	3.46 ± 0.06	5.79 ± 0.08
Granite	0.60 ± 0.01	N/A	N/A	N/A	4.98 ± 0.02

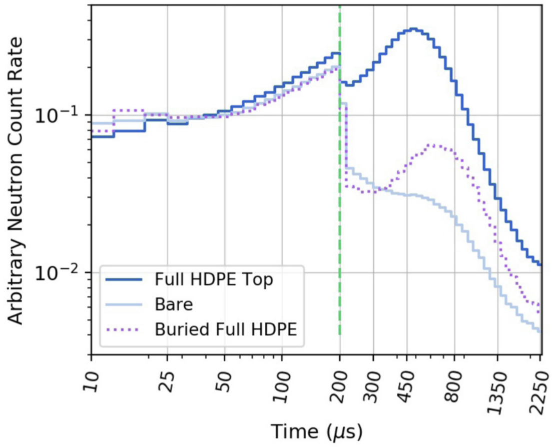

Fig. 7. Basalt monument neutron die-away curves comparing full HDPE top tiles, buried full HDPE tiles, and bare configurations. Comparison of the peaks (max count rate) of the neutron die-away curves in the thermal region (200–2250 μs) show a clear count suppression and time shift from the earlier time bins (full HDPE top, dark blue line, peak ≈ 470 μs) to the later time bins (buried full HDPE, purple dotted line, peak ≈ 620 μs) due to the buried H-rich material.

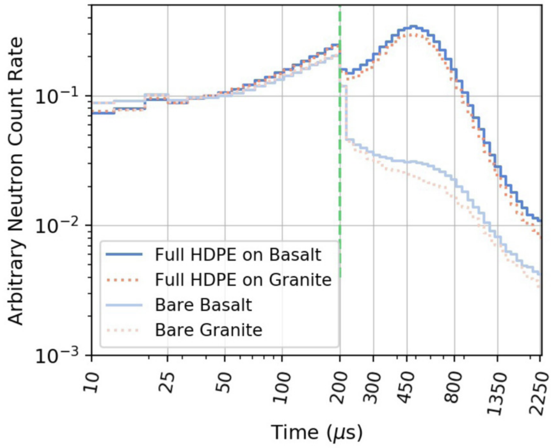

Fig. 8. Basalt and granite monument neutron die-away curves comparing full HDPE tile and bare configurations. Initial comparison of the magnitude of the neutron die-away curves show that the granite peaks are slightly suppressed for both configurations. Basalt and granite monuments with the full HDPE tile configurations show minor possible differences in shape.

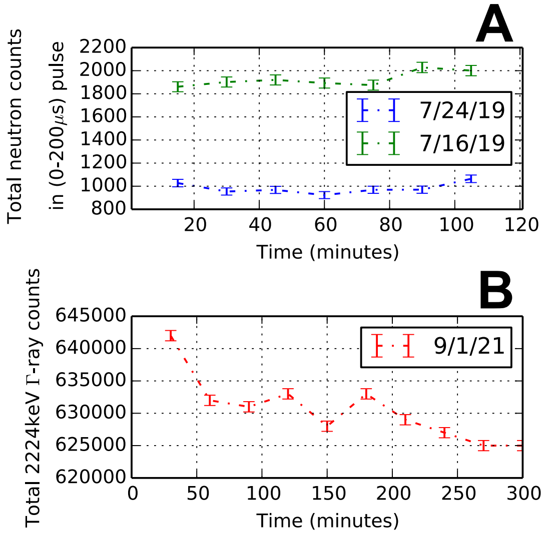

Fig. 9. Investigation of PNG pulse stability using (A) SINGR (2" CLYC) neutrons and (B) CeBr gamma rays. SINGR data (A) was taken on two different dates (2 hr measurements each) on top of the bare basalt monument, note that the 7/24/19 data was measured from an additional 6" vertical distance compared to the 7/16/19 data. The total neutron counts were divided into 15 min intervals during the neutron pulse period (0–200 μs). The variations between individual measurements/15 min in each data set for (A) are within 3%. The CeBr data (B) was taken at a much later date (9/1/21) and was also taken on top of the bare basalt monument (5 h total measurement) along with HDPE and a ≈5 lbs bag of table salt (NaI). The total gamma-ray data was divided into 30 min intervals, tracking the 2224 keV H peak. The measurement variation in (B) is within 3%. See Section 4.4 for further details.

more recent measurement (9/1/21) with a CeBr detector, along with HDPE and a ≈5 lbs bag of table salt (NaI). For each measurement, two hours of data was taken using SINGR, the data was then post-processed into neutron counts using PSD, then divided into 15 min chunks. These chunks were then divided into the 64 log-normal time bins, then the total number of counts from 0–200 μs (during the pulse) were integrated, Fig. 9(A) shows the results of this study. A five-hour data set was taken with a CeBr detector, which recorded gamma-ray data as a function of time; the total counts in the 2224 keV H peak was monitored in 30 min chunks, Fig. 9(B). This specific gamma-ray energy was chosen because it is the most prominent and is well isolated from other peaks. We used this information as a proxy for the stability over time of our PNG. The measurement variations in Fig. 9 (A) and (B) are within 3%. The downward trend in Fig. 9(B) may be due to the diffusion of deuterons or tritons out of the target as the temperature increases, but nevertheless the output is quite stable.

5. Comparison to simulation studies

Experimental results were compared to simulated results using both thermal (Fig. 10A–C, Fig. 11, Fig. 13, Fig. 14) and pulse-region normalization (Fig. 10D - F); they are presented with a focus on the thermal neutron region of the die-away curve (200–2250 μs).

Our experimental results confirm that the magnitude (Fig. 10A) and shape (Fig. 10D) of the neutron die-away curve changes for low amounts of H (0 to 0.25 wt% H in top 10 cm layer with single HDPE tile) for the bare and single HDPE tile configurations on the basalt monument. MCNP 6.1 is used to simulate the HDPE configurations (Fig. 10B & Fig. 10E) as well as the bare configuration with variable wt% H throughout the monument (no HDPE tiles, Fig. 10C & Fig. 10F). Our simulations confirm that both shape and magnitude of the thermal region of the neutron die-away curve change for low amounts of H (<0.25 wt% H in top 15 cm layer with single HDPE tile). However, for higher amounts of H (>0.5 wt% H in top 15 cm layer basalt with HDPE tiles on top), the thermal region normalized curves are no longer distinguishable between experimental measurements with three or more HDPE tiles (Fig. 10D) or simulated measurements (Fig. 10E & Fig. 10F). Our goodness-of-fit testing included over fitting, potentially due to over-parameterizing the model space (e.g. we did not need to run models of increase in wt% H for the full HDPE tile on top

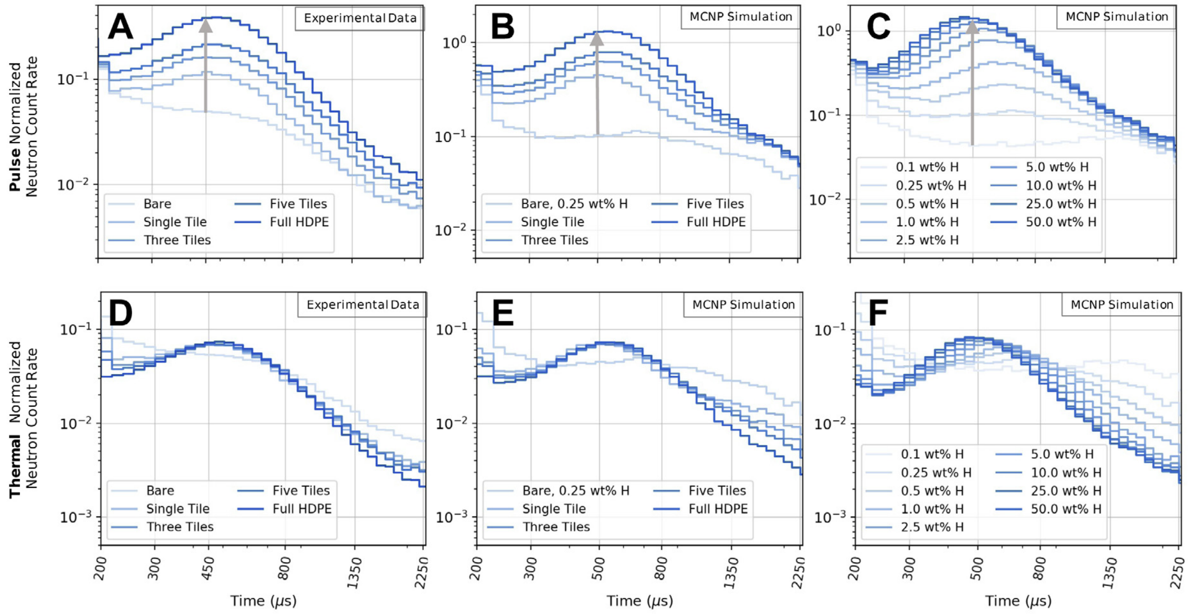

Fig. 10. Neutron die-away curves showing experimental results and simulated results side by side, focused on the neutron die-away region (200–2250 μs). (A & D) The basalt monument experiment using the HDPE configurations described in Fig. 3. (B & E) MCNP 6.1 simulations of the HDPE configurations on the basalt monument with 0.25 wt% H throughout the basalt. (C & F) MCNP 6.1 simulations of the bare (no HDPE tiles modeled) monument with change in H from 0–50 wt % throughout the basalt. Note that curves (A)–(C) are normalized to the PNG output pulse region (0–200 μs), and curves (D)–(F) are normalized to the thermal neutron return region (330 - 900 μs). The magnitude of the die-away curve in the thermal region is expected to increase as wt% H increases (gray arrows), as shown in the pulse normalized plots (A–C). The shape of the die-away curve is expected to change from 0–2.5 wt% H, shifting slightly from right to left time bins. The change in shape is shown in plots D & E between bare and single HDPE tile curves; the change in shape for plot F is seen in light blue curves from 0–2.5 wt % H.

Table 4
Best fit (χ^2-values, χ^2/m-values) statistics between experiment for full tile HDPE on top of the basalt monument and the associated MCNP model with variable wt% H in the basalt monument. Bins are endpoint inclusive normalized from bin 22/63 to bin 44/63, with a total number of degrees of freedom of 23.

wt% H	χ^2	χ^2/m	*Average %MCNP error*
0.0	20.43	0.97	0.017
0.5	22.35	1.06	0.018
1.0	23.08	1.10	0.018
2.0	25.38	1.21	0.018
3.0	27.33	1.30	0.019
4.0	27.75	1.32	0.019
5.0	27.71	1.32	0.019
6.0	28.34	1.35	0.019

configuration due to neutron sensing depth limits involving high-H content in upper layers). Over fitting occurs when the experiment and models are within the uncertainties of one another and the reduced chi-squared value is then interpreted as “fitting to the noise.” Alternative statistical methods for avoiding over-fitting with die-away data are discussed in the supplementary materials of Gabriel et al. 2018 [3].

5.1. HDPE top layer configurations

Fig. 11 shows the experimental neutron die-away curve from the full HDPE tiles on top of basalt compared to simulations using MCNP of the exact same configuration (full HDPE tiles on top). We found that the wt% H throughout the monument is indeterminable due to all χ^2/m-values < 1.5; these results are consistent with Feldman et al. 2000 [34] in regard to neutron sensing depth, such that SINGR’s sensing depth does not extend far past the top high-H layer. However, this does show that we can constrain our experimental data using simulations with a high-H top layer. An example of goodness-of-fit results of our MCNP study are shown in Table 4, with χ^2/m values visualized in Fig. 12 to find optimal fits for wt% H and burial depth of the HDPE layer.

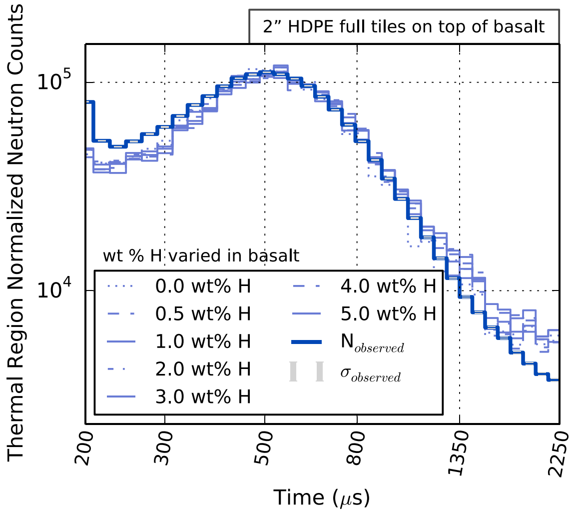

Fig. 11. Simulations compared to experiment for the full-tile HDPE top configuration on basalt. Experimental die-away curve results (deep blue, thick line) compared to MCNP output die-away curves for full tile HDPE top configuration on the basalt monument with varying amounts of H within the monument. The model output line colors reflect the χ^2/m-values when compared to the contour plot of Fig. 12; in this case all χ^2/m-values < 1.5. The MCNP models include the top layer of full HDPE tiles, wt% H is varied within the underlying basalt. The neutron counts in the time bins from 200–300 μs represent neutrons that may not be coming from the target surface but may be the result of interactions with nearby materials or instrument housings. Uncertainties in counts for simulation results are smaller than the plot line widths (<5% error, $< 0.02\%$ in thermal normalized region).

5.2. Buried HDPE configuration

We generated MCNP files for parametric studies of burial depth (0–24” by 2” increments), total wt% H (0–5 wt%) in the basalt, and thermal region normalized neutron count rate via die-away curves. Figs. 13

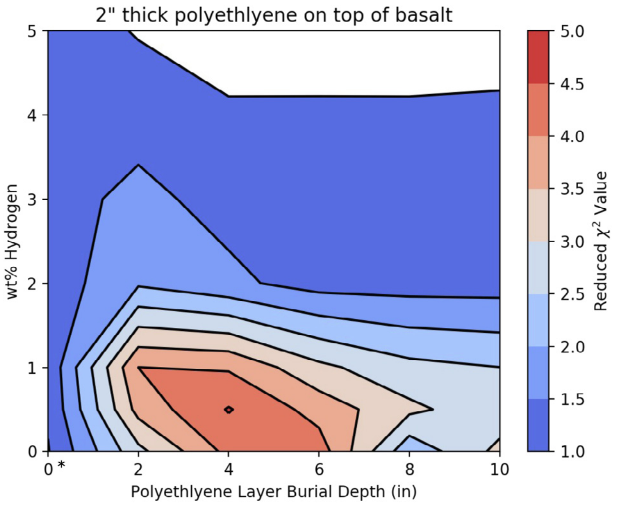

*0" burial depth corresponds to full HDPE tiles on top of the monument

Fig. 12. Reduced-χ^2 (χ^2/m) contour plot comparison of the full tile HDPE top experiment on basalt and associated MCNP simulations with change in wt% H and burial depth of HDPE. All curves were thermal region normalized. Cooler colors represent lower χ^2/m-values, implying better model-to-measurement fits; values of χ^2/m less than 1.5 are considered good fits between model and experiment. The white region represents an over-fitting (Section 5) where models and experiment are within the uncertainties of each other (i.e. χ^2/m test is "fitting to the noise"). As seen in Fig. 10(B), if the amount of H is very large, the shape of the thermal normalized neutron die-away curve becomes indistinguishable between measurements. This plot indicates that there is either 1) a high-H deposit on top of the monument (the experimental match, all χ^2/m-values are close to 1.0 for 2" thick HDPE 0" burial depth) and that there may be greater than 0 wt% H throughout the monument or 2) that there is greater than 2 wt% H throughout the monument regardless of 2" thick HDPE burial depth. This plot also indicates that a buried deposit of H under a dry (<2 wt% H) layer of basalt is unlikely ($\chi^2/\mathrm{m} > 2.5$) within neutron sensing depth limits (≈0.5 m in basalt, energy-dependent). (For interpretation of the references to color in this figure legend, the reader is referred to the web version of this article.)

and 14 show examples of these MCNP neutron die-away outputs for HDPE buried within the basalt monument. Fig. 13 shows varying 2" thick HDPE layer burial depths (0–10" depths shown) with 1 wt% H throughout all layers of basalt. Fig. 14 shows varying wt% H (0–5 wt%) throughout all layers of basalt with 2" thick HDPE buried at a depth of 6". Fig. 15 shows a contour plot from our MCNP parametric study of the 2" thick HDPE layer buried for distances 0–10", versus the wt% H distributed throughout the basalt monument, versus the χ^2/m-value between MCNP simulation and experiment, both of which were thermal region normalized. The models suggest that the wt% H content of this experiment is between 0.0–2 wt% H, with a 2" HDPE depth range of 4–10". These simulation results place accurate constraints on the actual experimental configuration (6" burial depth with ≈ 0.05 wt% H) and verify that the neutron die-away method can be used to constrain wt% H and depth for low-H environments (<0.5 wt% H).

Fig. 16C shows the result of the homogeneous model comparison of the buried HDPE configuration compared to basalt monument models with varying wt% H that do not contain HDPE. Note that Fig. 16C is plotted on a linear scale in order to emphasize the thermal neutron peak location. As noted in Section 5, the goodness-of-fit (χ^2/m) can suffer from over-fitting, though it may also suffer from sample-size issues, meaning that a larger sample size can cause trivial relationships to appear statistically significant; though outside the scope of this paper, methods discussed in the supplementary materials of Gabriel et al. 2018 [3] provide more rigorous methods of analysis to avoid these issues. It is clear in Fig. 16C that there is a time bin shift to the right (forward in time) due to burying the HDPE tiles, though a χ^2/m-value of <1.1 corresponds to a homogeneous model (1 wt% H).

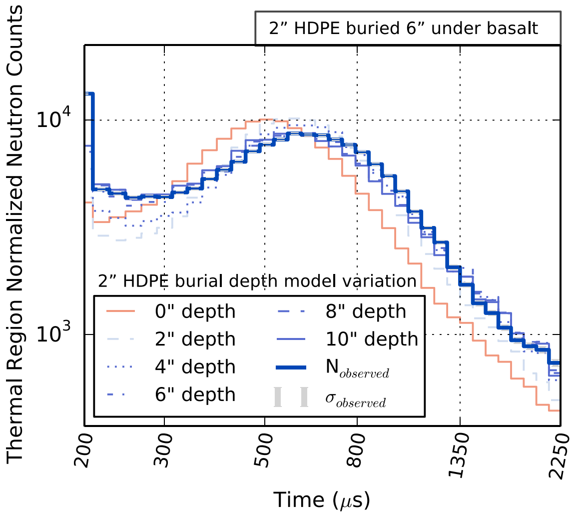

Fig. 13. Experimental die-away curve results (deep blue, thick line) for HDPE buried under 6" of basalt compared to MCNP output die-away curves for 2" thick HDPE under different burial depths of basalt. The model output line colors reflect the χ^2/m-values when compared to the contour plot of Fig. 15. All of the basalt contains 1 wt% H distributed throughout the bottom and top layers of the monument for this set of models. Values of χ^2/m less than 1.5 are considered good fits between model and experiment; for this set of models with 1 wt% throughout the basalt, a 2" HDPE layer is constrained to a depth of 6–10".

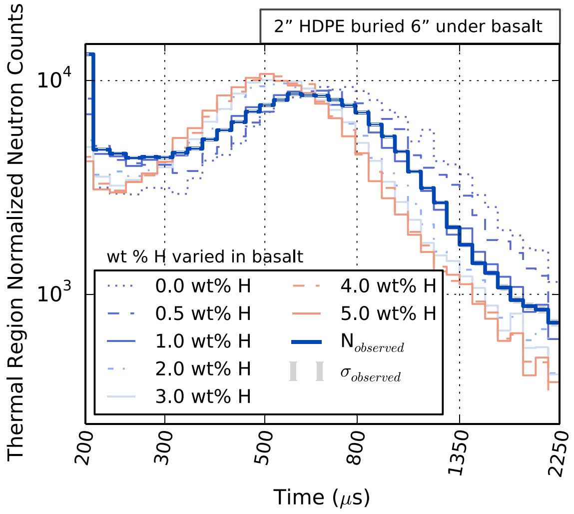

Fig. 14. Experimental die-away curve results (deep blue, thick line) for HDPE buried under 6" of basalt compared to MCNP output die-away curves. The model output line colors reflect the χ^2/m-values when compared to the contour plot of Fig. 15. The MCNP models consist of the buried 2" thick HDPE full-tile layer under 6" of basalt, with wt% H varied throughout the basalt both above and below the HDPE layer. For this set of models with a 2" HDPE layer modeled at a depth of 6", the wt% H in the basalt is constrained to 0.0–1.0 wt%.

5.3. *Bare monument configuration*

We compare the bare, full tile HDPE on top, and buried HDPE basalt monument configurations to MCNP simulations of only the bare basalt monument with varying wt % H, as shown in Fig. 16. The χ^2/m-values between MCNP simulations and experiment for the bare basalt monument (Fig. 16 A) are most consistent ($0.9 < \chi^2/\mathrm{m} < 1.4$) with models that have 0.6–1.3 wt% H throughout the basalt; this is not consistent with the assay of 0.05 wt% H reported by Bodnarick et al. 2013 [5]. The experiment for the full HDPE tiles on top of the basalt monument (Fig. 16 B) are most consistent ($1.5 < \chi^2/\mathrm{m} < 1.8$) with

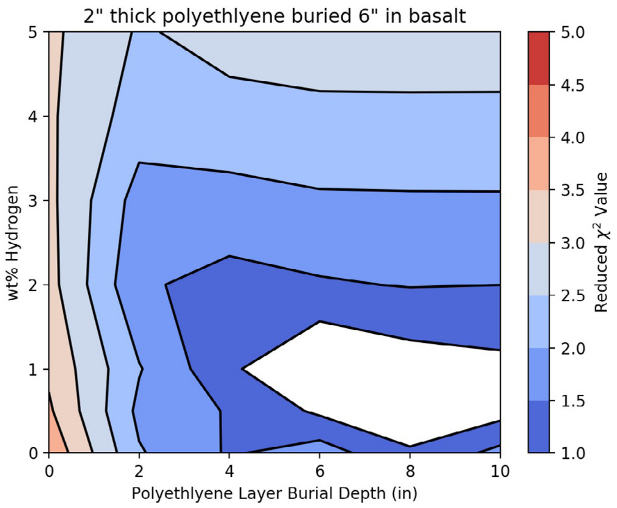

Fig. 15. Reduced-χ^2 (χ^2/m) contour plot of the 6'' buried HDPE experiment in basalt compared to MCNP simulations for change in wt% H versus burial depth of HDPE. The experiment is located at a 6'' burial depth with ≈ 0.05wt % H (from elemental assay performed in Bodnarick et al. 2013 [5]), which is reflected in the over fitted region of the contour plot (white area, see Section 5 for details). Values of χ^2/m less than 1.5 are considered good fits between model and experiment.

models that have 2.5–10 wt% H throughout the basalt; all of the χ^2/m-values for this study are greater than 1.0, suggesting that the H is unlikely to be distributed throughout the monument. The experiment for the full HDPE tiles buried 6'' under basalt in the monument (Fig. 16 C) are most consistent ($0.85 < \chi^2/\mathrm{m} < 1.26$) with models that have 0.25–2.0 wt% H throughout the basalt. This is consistent with the range of H values given in Table 2 for the full-tile monument, from 0.08 wt% H in the full monument to 1.57 wt% H in the top 15 cm of the monument.

6. Discussion

6.1. High-hydrogen environments

From the HDPE configuration tests (Figs. 6 and 10), we observed that as the wt% H increases beyond 0.25 wt% (2.25 wt% WEH) in the top 15 cm (more than a single HDPE tile), the shape of the neutron die-away curve becomes indistinguishable between measurements and only the magnitude allows for wt% H estimation. This is consistent with our MCNP simulation studies (Fig. 10) and similar to simulation studies by Kerner et al. 2020 [1] for low Σ_a compositions. Studies by Feldman et al. 2000 [34] show maximum peak neutron density at a mixture of 3 wt% WEH by mass (0.33 wt% H) in a ferroan-anorthosite material ($\Sigma_a \approx 0.06$ cm^{-1}); this agrees well with our results, given that both the basalt and granite monuments have low Σ_a.

The macroscopic thermal neutron cross sections of the basalt and granite monuments are similar and are considered low in comparison to those calculated for other planetary compositions [1]. For measurements with similar low-Σ_a and high-H (HDPE top tiles configuration) compositions, as shown in Fig. 8, the shape of the neutron die-away curve does not dramatically change. However, as shown in Table 3, the bare granite and basalt monuments have clearly different count rates, though both sets of die-away curves are statistically similar when thermal region normalized ($\chi^2/\mathrm{m} = 0.99$, $\chi^2/\mathrm{m} = 0.73$ for bare and full HDPE tiles, respectively). From our data, we infer that materials with more subtle differences (<0.01 cm^{-1} difference) in absorption cross section may be indeterminable when buried under high-H materials. Simulation studies on Mars compositions ($\Sigma_a > 0.005$ cm^2/g or 0.2 cm^{-1}) done by Kerner et al. 2020 [1] and data collected by MSL DAN [2,3] have shown that neutron die-away can be used to characterize higher-H (>2.5 wt% WEH in top 15 cm) abundances when the local rocks and soils contain materials with higher thermal neutron macroscopic absorption cross section (i.e. due to elevated Fe and Cl abundances on Mars). As shown in Fig. 10(C/F), high-H environments begin to show much more subtle changes in the die-away shape, requiring more reliance on the magnitude of the pulse-region normalized data.

6.2. Simulations can be used to constrain results

Fig. 10 shows the results of our MCNP simulation studies of neutron die-away on the basalt monument. The change in the shape of the neutron die-away curves matches well between experiment and simulations as demonstrated with the HDPE full tile on top and buried HDPE configurations. We constrained the HDPE top layer to be in the top 0–2'' of the monument (for 0–2 wt% H), but were unable to fully constrain the underlying H wt% content of the basalt due to neutron sensing depth limitations (Fig. 12). We constrained the buried HDPE layer to be buried within 4–10'', with the basalt top layer containing 0–2 wt% H within the constrained burial depth of the HDPE (Fig. 15).

Further discrepancies between simulation and experiment may include small distance uncertainties, atmospheric moisture changes, and the layering of bricks of the basalt and granite monuments (in which rain water can seep and sometimes pool between the brick or buried HDPE layers). This is evident in our experimental comparisons to simulations, where we see a variation of 0.1–2 wt% H in bare basalt. Measurements were taken in Maryland, USA, from May–August, when humidity can range from 50%–90%, although no measurements were taken during rainfall.

6.3. CLYC benefits and drawbacks

CLYC's greatest benefit, and therefore SINGR's greatest benefit, is that it is capable of detecting both neutrons and gamma rays. Throughout our experiments, we confirmed that CLYC is efficient at both small and large volumes for neutron detection; neutron die-away was easily achievable using 2'' CLYC. However, for active dual use on planetary science missions, larger CLYC crystals (>2'') would provide higher count rate statistics (decreasing the necessary integration time) and more efficient high-energy sensitivity to gamma rays. While we were unable to collect active gamma-ray spectra using 2'' CLYC with a PNG, we were able to collect typical passive gamma-ray data with standard lab sources (^{60}Co, ^{137}Cs). A preliminary measurement with a larger crystal (3'') shows that active gamma-ray acquisition is possible with CLYC [46].

CLYC is not without drawbacks, like many planetary science instruments, radiation and thermal damage can degrade the detection efficiency of CLYC for both gamma rays and neutrons (light dimming); however, this damage degrades resolution for gamma rays only. Both damage mechanisms can be partially repaired through the use of room-temperature annealing [31,42,47–49]. Unlike HPGe detectors, annealing of scintillator crystals–such as CLYC–does not result in active volume loss and efficiency degradation [50].

Much of the efficiency loss experienced by the SINGR system was likely due to the high neutron event rate causing pulse pile-up (particles hitting the crystal at the same time saturate the detector and the signals become difficult to individually count); this pulse pile-up effect may also explain the slightly distorted PSD plot shown in Fig. 5. The decay constants of CLYC are 1–1000 ns (Table 1), which are fairly long in comparison to other GRNS ($NaI(Tl) \approx 250$ ns), which is likely why the detector would saturate while taking data during the neutron pulse.

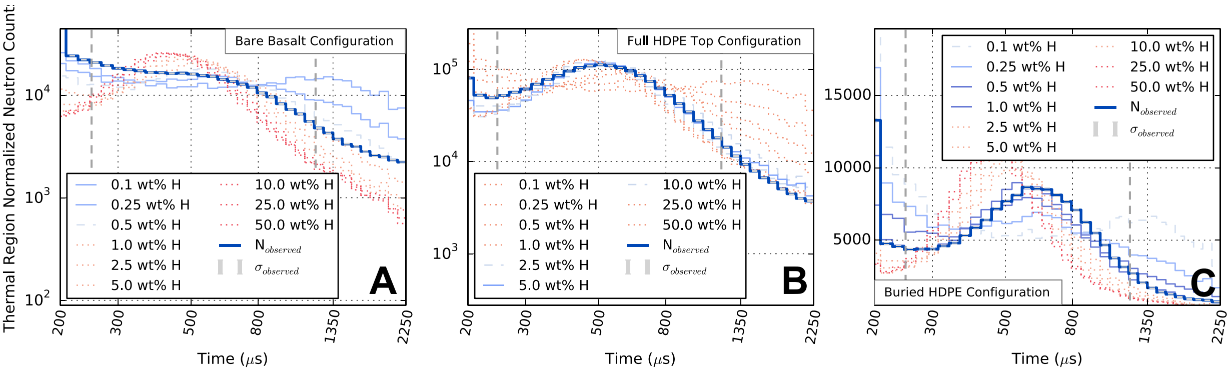

Fig. 16. MCNP bare basalt monument configuration simulations compared side by side to experimental measurements on the basalt monument for (A) the bare configuration, (B) the full HDPE tiles on top configuration, and (C) the buried full HDPE tiles configuration. The basalt monument is modeled with increasing amounts of wt% H from 0.1–50.0 throughout the basalt, there is no HDPE present in the models, these are homogeneous, single layer models (see Section 5.3). The experimental measurement (observed value) is shown as a deep blue, thick line, the model output line colors reflect the χ^2/m-values using the same color scale as Figs. 12 and 15 . The vertical, gray, dotted lines represent time bins 22–44, which are used for χ^2/m comparison and thermal region normalization. The bare basalt monument models for 0.1–0.5 wt% H agree moderately well (χ^2/m < 2.0) with the bare experimental measurement in (A); this is within the value of the elemental assay (0.5 wt% H) done by Bodnarick et al. 2013 [32]. In (B) 2.5–10 wt% H model results have χ^2/m-values < 2.0 as compared to the experimental measurement (see Section 6.1). In (C) the y-scale is linear to show the shift in the time bins for the thermal neutron peak (see Section 5.2); 0.1–1.0 wt% H model results have χ^2/m-values < 2.0 as compared to the experimental measurement. (For interpretation of the references to color in this figure legend, the reader is referred to the web version of this article.)

7. Summary

We generated neutron die-away curves using SINGR and a PNG. Six different experimental HDPE geometry configurations were used to simulate an increase in wt% H abundance, along with one buried HDPE configuration to demonstrate H distribution with depth. Results show that the measurements can constrain the depth of buried H-rich material.

We conclude that SINGR can be used to inform near-surface (within the top 15 cm) H content in a variety of environments. With a PNG, the integrated thermal neutron albedo can be used to estimate the H abundance. Additional information about the near-surface neutron absorbing elements can be gained through analysis of the neutron die-away curve shape for low-H environments (<0.25 wt% H) between compositions that have sufficiently different (>0.01 cm^{-1} difference) macroscopic thermal neutron absorption cross sections.

Qualitatively, we confirm that the shape of the neutron die-away curve changes significantly for low amounts of H (0–0.25 wt% H in top 15 cm). However, for high amounts of H (>0.25 wt% H in top 15 cm), the curves normalized to the thermal neutron count rate are no longer distinguishable between measurements (Fig. 10 D–F for one or more HDPE tiles) with the same underlying material. At high-H abundance, the total magnitude of the thermal neutron die-away curve is the main indicator of H content. In the absence of information about the neutron output of the PNG, the shape of the thermal neutron die-away curve can be used to determine low-H abundance (<0.25 wt% H) and inform macroscopic thermal neutron cross section information; however, as determined by MSL DAN, normalized curves require additional counting statistics and longer integration times [3].

Due to the reduced effect on curve shape in high-H environments, it is important to monitor the neutron output of the PNG for determination of bulk H content. This would enable more robust reduction of raw neutron die-away data without requiring thermal region normalization. Over our two months of measurements, our results did not show significant changes in the PNG output pulse. However, results from the DAN instrument on Mars determined that the PNG neutron output degrades over time due to the degradation of the fill gas and the half-life of tritium [51]. Our results contribute to the argument for a need to monitor the PNG output, during the duration of the mission, to determine the absolute number of neutrons emitted from the PNG during measurements, particularly when analyzing non-normalized data products.

We were unable to generate efficient time-resolved (active) gamma-ray spectra using a 2” CLYC crystal, likely due to the detector’s small volume (2” long x 2” diameter). SINGR experienced a saturation of events (likely due to high neutron event rate) during the neutron generator pulse, which also contributed to the efficiency degradation for gamma-ray measurements. Larger CLYC crystals for active gamma-ray measurements, as well as similar elpasolite scintillators (e.g., CLLBC ($Cs_2LiLa(Br,Cl)_6 : Ce$) and TLYC ($Tl_2LiYCl_6 : Ce$)), which exist with shorter light decay times, may be required to reduce the significance of pulse pileup in SINGR active gamma-ray data. TLYC also has a higher density than CLYC, making it more likely to be an efficient gamma-ray spectrometer (though its resolution is worse compared to CLYC) [52]. Still, we conclude that SINGR (2” CLYC) has the potential to be used successfully for active neutron measurements on planetary bodies, with the addition of passive gamma-ray and neutron measurements [13].

CRediT authorship contribution statement

L.E. Heffern: Conceptualization, Methodology, Software, Formal analysis, Investigation, Data curation, Writing – original draft, Writing – review & editing, Visualization, Project administration. **C.J. Hardgrove:** Writing – original draft, Writing – review & editing, Supervision, Resources, Project administration, Funding acquisition, Visualization. **A. Parsons:** Supervision, Resources, Project administration, Funding acquisition, Visualization, Investigation, Methodology. **E.B. Johnson:** Supervision, Resources, Investigation, Software, Writing – review & editing. **R. Starr:** Supervision, Investigation, Writing – review & editing, Methodology. **G. Stoddard:** Data curation, Software. **R.E. Blakeley:** Investigation, Software. **T. Prettyman:** Visualization, Writing – review & editing. **T.S.J. Gabriel:** Visualization, Writing – original draft, Writing – review & editing. **H. Barnaby:** Writing – review & editing. **J. Christian:** Conceptualization, Writing – review & editing. **M.A. Unzueta:** Methodology, Validation, Investigation. **C. Tate:** Methodology, Software, Writing – review & editing, Investigation. **A. Martin:** Methodology, Investigation. **J. Moersch:** Conceptualization, Methodology.

Declaration of competing interest

The authors declare that they have no known competing financial interests or personal relationships that could have appeared to influence the work reported in this paper.

Acknowledgments

The authors acknowledge Research Computing at Arizona State University for providing resources that have contributed to the research results reported within this paper (URL: http://www.researchcomputing.asu.edu). The authors would also like to thank Steven Dibb from Arizona State University for MCNP debugging assistance. Any use of trade, firm, or product names is for descriptive purposes only and does not imply endorsement by the U.S. Government.

Funding

This project was funded by a grant from NASA via The Planetary Instrument Concepts for the Advancement of Solar System Observations (PICASSO) Program, which supports the development of spacecraft-based instrument systems that show promise for use in future planetary missions [NNH14ZDA001N-PICASSO].

References

[1] H.R. Kerner, C.J. Hardgrove, S. Czarnecki, T.S.J. Gabriel, I.G. Mitrofanov, M.L. Litvak, A.B. Sanin, D.I. Lisov, Analysis of active neutron measurements from the mars science laboratory dynamic albedo of neutrons instrument: Intrinsic variability, outliers, and implications for future investigations, J. Geophys. Res. Planets 125 (5) (2020) e2019JE006264.

[2] S. Czarnecki, C.J. Hardgrove, P.J. Gasda, T.S.J. Gabriel, M. Starr, M.S. Rice, J. Frydenvang, R.C. Wiens, W. Rapin, S. Nikiforov, D. Lisov, M. Litvak, F. Calef, H. Gengl, H. Newsom, L. Thompson, S. Nowicki, Identification and description of a silicic volcaniclastic layer in Gale crater, Mars, using active neutron interrogation, J. Geophys. Res. Planets 125 (3) (2020) e2019JE006180.

[3] T.S.J. Gabriel, C.J. Hardgrove, S. Czarnecki, E.B. Rampe, W. Rapin, C.N. Achilles, D. Sullivan, S. Nowicki, L. Thompson, M. Litvak, I. Mitrofanov, R.T. Downs, Water abundance of dunes in Gale crater, Mars from active neutron experiments and implications for amorphous phases, Geophys. Res. Lett. 45 (23) (2018) 12,712–766,775.

[4] M.L. Litvak, D.V. Golovin, A.B. Kolesnikov, A.A. Vostrukhin, M.V. Djachkova, A.S. Kozyrev, I.G. Mitrofanov, M.I. Mokrousov, A.B. Sanin, Ground-based measurements with the ADRON active gamma-ray and neutron spectrometer designed for lunar and Martian landing missions, Sol. Syst. Res. 51 (3) (2017) 171–184.

[5] J. Bodnarik, D. Burger, A. Burger, L. Evans, A. Parsons, J. Schweitzer, R. Starr, K. Stassun, Time-resolved neutron/gamma-ray data acquisition for in situ subsurface planetary geochemistry, Nucl. Instrum. Methods Phys. Res. A 707 (2013) 135–142.

[6] A. Parsons, T. McClanahan, J. Bodnarik, L. Evans, S. Nowicki, J. Schweitzer, R. Starr, Subsurface In situ elemental composition measurements with PING, in: IEEE Aerospace Conference Proceedings, 2013.

[7] S.F. Nowicki, L.G. Evans, R.D. Starr, J.S. Schweitzer, S. Karunatillake, T.P. McClanahan, J.E. Moersch, A.M. Parsons, C.G. Tate, Modeled Martian subsurface elemental composition measurements with the probing In situ with neutron and Gamma ray instrument, Earth Space Sci. 4 (2) (2017) 76–90.

[8] C. Hardgrove, J. Moersch, D. Drake, Effects of geochemical composition on neutron die-away measurements: Implications for Mars Science Laboratory's dynamic albedo of neutrons experiment, Nucl. Instrum. Methods Phys. Res. A 659 (1) (2011) 442–455.

[9] A. Parsons, M. Burks, D.J. Lawrence, R.D. Lorenz, R. Miller, P.N. Peplowski, L. Perkins, E.P. Turtle, The Dragonfly Gamma-ray and neutron spectrometer (DraGNS): Elemental composition measurements on the surface of Titan, in: AGU Fall Meeting Abstracts, 2018, P52C-08.

[10] I.G. Mitrofanov, M.L. Litvak, A.B. Varenikov, Y.N. Barmakov, A. Behar, Y.I. Bobrovnitsky, E.P. Bogolubov, W.V. Boynton, K. Harshman, E. Kan, A.S. Kozyrev, R.O. Kuzmin, A.V. Malakhov, M.I. Mokrousov, S.N. Ponomareva, V.I. Ryzhkov, A.B. Sanin, G.A. Smirnov, V.N. Shvetsov, G.N. Timoshenko, T.M. Tomilina, V.I. Tret'yakov, A.A. Vostrukhin, Dynamic albedo of neutrons (DAN) experiment onboard NASA's Mars Science Laboratory, Space Sci. Rev. 170 (1) (2012) 559–582.

[11] M.L. Litvak, I.G. Mitrofanov, Y. Barmakov, A. Behar, A. Bitulev, Y. Bobrovnitsky, E.P. Bogolubov, W.V. Boynton, S.I. Bragin, S. Churin, A.S. Grebennikov, A. Konovalov, A.S. Kozyrev, I.G. Kurdumov, A. Krylov, Y. Kuznetsov, A.V. Malakhov, M.I. Mokrousov, V.I. Ryzhkov, A.B. Sanin, V.N. Shvetsov, G.A. Smirnov, S. Sholeninov, G.N. Timoshenko, T.M. Tomilina, D.V. Tuvakin, V.I. Tretyakov, V.S. Troshin, V.N. Uvarov, A. Varenikov, A. Vostrukhin, The dynamic albedo of neutrons (DAN) experiment for NASA's 2009 Mars Science Laboratory, Astrobiology 8 (3) (2008) 605–612.

[12] E.B. Johnson, C. Whitney, S. Vogel, J.F. Christian, K. Holbert, P. Chandhran, High event rate, pulse shape discrimination algorithm for CLYC, in: 2015 IEEE International Symposium on Technologies for Homeland Security, HST, 2015, pp. 1–7.

[13] J. Glodo, R. Hawrami, E. van Loef, U. Shirwadkar, K.S. Shah, Pulse shape discrimination with selected elpasolite crystals, IEEE Trans. Nucl. Sci. 59 (5) (2012) 2328–2333.

[14] A. Parsons, J. Bodnarik, L. Evans, S. Floyd, L. Lim, T. McClanahan, M. Namkung, S. Nowicki, J. Schweitzer, R. Starr, J. Trombka, Active neutron and gamma-ray instrumentation for in situ planetary science applications, in: Nucl. Instrum. Methods Phys. Res. A, 652 (1) (2011) 674–679.

[15] A. Parsons, J. Bodnarik, L. Evans, T. McClanahan, R. Starr, The Probing In-Situ With Neutron and Gamma Rays (PING) Instrument for Planetary Composition Measurements, Technical Report, 2012.

[16] D.J. Lawrence, S. Fix, J.O. Goldsten, S.V. Heuer, R.S. Hourani, S. Kerem, P.N. Peplowski, Near-space operation of compact CsI, CLYC, and CeBr3 sensors: Results from two high-altitude balloon flights, Nucl. Instrum. Methods Phys. Res. A 905 (2018) 33–46.

[17] C. Hardgrove, R. Starr, I. Lazbin, A. Babuscia, B. Roebuck, J. Dubois, N. Struebel, A. Colaprete, D. Drake, E. Johnson, J. Christian, L. Heffern, S. Stem, S. Parlapiano, M. Wiens, A. Genova, D. Dunham, D. Nelson, B. Williams, J. Bauman, P. Hailey, T. Obrien, K. Marwah, L. Vlieger, J. Bell, T. Prettyman, T. Crain, E. Cisneros, N. Cluff, G. Stoddard, M. Kaffine, The lunar polar hydrogen mapper CubeSat mission, IEEE Aerosp. Electron. Syst. Mag. 35 (3) (2020) 54–69.

[18] D. David Schechtman Stonehill, L. Catherine Mesick, K. Elizabeth Dunn, J. Philip, D.D. S, The SENSER CLYC experiment, in: IEEE Nuclear Science Symposium and Medical Imaging Conference, 2016.

[19] G.F. Knoll, Radiation Detection and Measurement, fourth ed., Wiley, New York, NY, 2010.

[20] A. Vertes, S. Nagy, K. Suvegh, Nuclear Methods in Mineralogy and Geology, Springer, US, 1998.

[21] V. Ferronsky, Nuclear Geophysics: Applications in Hydrology, Hydrogeology, Engineering Geology, Agriculture and Environmental Science, Springer International Publishing, 2015, pp. 1–522.

[22] Specification Sheet: RIIDEye Series, ThermoFisher Scientific, 2012, URL: https://www.thermofisher.com/.

[23] W.C. Feldman, B.L. Barraclough, K.R. Fuller, D.J. Lawrence, S. Maurice, M.C. Miller, T.H. Prettyman, A.B. Binder, The lunar prospector gamma-ray and neutron spectrometers, Nucl. Instrum. Methods Phys. Res. A 422 (1–3) (1999) 562–566.

[24] Detective X Ultra High Resolution HPGe Radioisotope Identification Device The New "Gold Standard" for Mission Critical Detection and Identification, Ortec, 2018, URL: https://www.ortec-online.com/.

[25] M.T. Burks, O.B. Drury, J.O. Goldsten, L.B. Hagler, L.E. Heffern, N.R. Hines, G.-B. Kim, D.J. Lawrence, K.E. Nelson, P.N. Peplowski, Z.W. Yokley, GeMini: A high-resolution, low-resource, Gamma-ray spectrometer for planetary science applications, Space Sci. Rev. 216 (7) (2020) 1–23.

[26] CLYC Gamma-Neutron Scintillator, RMD Inc, 2021, URL: https://www.dynasil.com/product-category/scintillators/clyc-gamma-neutron-scintillators/.

[27] N. D'Olympia, P. Chowdhury, C. Lister, J. Glodo, R. Hawrami, K. Shah, U. Shirwadkar, Pulse-shape analysis of CLYC for thermal neutrons, fast neutrons, and gamma-rays, Nucl. Instrum. Methods Phys. Res. A 714 (2013) 121–127, http://dx.doi.org/10.1016/J.NIMA.2013.02.043.

[28] D. Pérez-Loureiro, O. Kamaev, G. Bentoumi, L. Li, C. Jewett, M. Thompson, Evaluation of CLYC-6 and CLYC-7 scintillators for detection of nuclear materials, Nucl. Instrum. Methods Phys. Res. A 1012 (2021) 165622, http://dx.doi.org/10.1016/J.NIMA.2021.165622.

[29] N. Dolympia, P. Chowdhury, C.J. Guess, T. Harrington, E.G. Jackson, S. Lakshmi, C.J. Lister, J. Glodo, R. Hawrami, K. Shah, U. Shirwadkar, Optimizing Cs2LiYCl6 for fast neutron spectroscopy, Nucl. Instrum. Methods Phys. Res. A 694 (2012) 140–146, http://dx.doi.org/10.1016/J.NIMA.2012.07.021.

[30] Thermo Scientific MP 320, Thermo Fisher Scientific Inc, 2007, URL: https://www.thermofisher.com/document-connect/document-connect.html?url=https.

[31] D.D. Coupland, B.S. Budden, L.C. Stonehill, Thermal variance investigation and scintillation mechanisms of Cs2LiLaBr6-xClx:Ce (CLLBC) and Cs2LiYBr6:Ce (CLYB), in: 2015 IEEE Nuclear Science Symposium and Medical Imaging Conference, NSS/MIC 2015, Institute of Electrical and Electronics Engineers Inc, 2016.

[32] J.G. Bodnarik, Physics Using In Situ Neutron And Gamma-Ray Spectroscopy (Ph.D. thesis), Graduate School of Vanderbilt University, 2013.

[33] Compendium of material composition data for radiation transport modeling | PNNL, 2021, URL: https://www.pnnl.gov/publications/compendium-material-composition-data-radiation-transport-modeling-1.

[34] W.C. Feldman, D.J. Lawrence, R.C. Elphic, D.T. Vaniman, D.R. Thomsen, B.L. Barraclough, S. Maurice, A.B. Binder, Chemical information content of lunar thermal and epithermal neutrons, J. Geophys. Res. Planets 105 (E8) (2000) 20347–20363.

[35] W. Thompson, MCNP, a general Monte Carlo Code for Neutron and Photon Transport: A Summary, Technical Report, Los Alamos National Laboratory (LANL), 1979.

[36] M.C. Team, MCNP-A General Monte Carlo N-Particle Transport Code, Version 5 Volume I: Overview and Theory X-5 Monte Carlo Team, LANL, 2003, pp. 1–6–1–12.

[37] G. Van Rossum, F. Drake, The Python Reference Manual, (March) Centrum voor Wiskunde en Informatica Amsterdam, 1995, URL: www.python.org.

[38] P. Virtanen, R. Gommers, T.E. Oliphant, M. Haberland, T. Reddy, D. Cournapeau, E. Burovski, P. Peterson, W. Weckesser, J. Bright, S.J. van der Walt, M. Brett, J. Wilson, K.J. Millman, N. Mayorov, A.R. Nelson, E. Jones, R. Kern, E. Larson, C. Carey, I. Polat, Y. Feng, E.W. Moore, J. VanderPlas, D. Laxalde, J. Perktold, R. Cimrman, I. Henriksen, E. Quintero, C.R. Harris, A.M. Archibald, A.H. Ribeiro, F. Pedregosa, P. van Mulbregt, A. Vijaykumar, A.P. Bardelli, A. Rothberg, A. Hilboll, A. Kloeckner, A. Scopatz, A. Lee, A. Rokem, C.N. Woods, C. Fulton, C. Masson, C. Häggström, C. Fitzgerald, D.A. Nicholson, D.R. Hagen, D.V. Pasechnik, E. Olivetti, E. Martin, E. Wieser, F. Silva, F. Lenders, F. Wilhelm, G. Young, G.A. Price, G.L. Ingold, G.E. Allen, G.R. Lee, H. Audren, I. Probst, J.P. Dietrich, J. Silterra, J.T. Webber, J. Slavič, J. Nothman, J. Buchner, J. Kulick, J.L. Schönberger, J.V. de Miranda Cardoso, J. Reimer, J. Harrington, J.L.C. Rodríguez, J. Nunez-Iglesias, J. Kuczynski, K. Tritz, M. Thoma, M. Newville, M. Kümmerer, M. Bolingbroke, M. Tartre, M. Pak, N.J. Smith, N. Nowaczyk, N. Shebanov, O. Pavlyk, P.A. Brodtkorb, P. Lee, R.T. McGibbon, R. Feldbauer, S. Lewis, S. Tygier, S. Sievert, S. Vigna, S. Peterson, S. More, T. Pudlik, T. Oshima, T.J. Pingel, T.P. Robitaille, T. Spura, T.R. Jones, T. Cera, T. Leslie, T. Zito, T. Krauss, U. Upadhyay, Y.O. Halchenko, Y. Vázquez-Baeza, SciPy 1.0: Fundamental algorithms for scientific computing in Python, Nature Methods 17 (3) (2020) 261–272.

[39] W. Mckinney, Data structures for statistical computing in Python, Technical Report, 2010.

[40] C.R. Harris, K.J. Millman, S.J. van der Walt, R. Gommers, P. Virtanen, D. Cournapeau, E. Wieser, J. Taylor, S. Berg, N.J. Smith, R. Kern, M. Picus, S. Hoyer, M.H. van Kerkwijk, M. Brett, A. Haldane, J.F. del Río, M. Wiebe, P. Peterson, P. Gérard-Marchant, K. Sheppard, T. Reddy, W. Weckesser, H. Abbasi, C. Gohlke, T.E. Oliphant, Array programming with NumPy, Nature 585 (7825) (2020) 357–362.

[41] A. Mentana, F. Camera, A. Giaz, N. Blasi, S. Brambilla, S. Ceruti, L. Gini, F. Groppi, S. Manenti, B. Million, S. Riboldi, To cite this article: A Mentana et al., J. Phys. Conf. Ser. 763 (2016) 12006.

[42] K. Mesick, K. Bartlett, D. Coupland, L. Stonehill, Effects of proton-induced radiation damage on CLYC and CLLBC performance, Nucl. Instrum. Methods Phys. Res. A 948 (C) (2019).

[43] G.R. Gilmore, Practical Gamma-Ray Spectrometry: Second Edition, John Wiley and Sons, 2008, pp. 118–122.

[44] I.G. Mitrofanov, M.L. Litvak, A.B. Sanin, R.D. Starr, D.I. Lisov, R.O. Kuzmin, A. Behar, W.V. Boynton, C. Hardgrove, K. Harshman, I. Jun, R.E. Milliken, M.A. Mischna, J.E. Moersch, C.G. Tate, Water and chlorine content in the martian soil along the first 1900 m of the curiosity rover traverse as estimated by the DAN instrument, J. Geophys. Res. Planets 119 (7) (2014) 1579–1596.

[45] A.B. Sanin, I.G. Mitrofanov, M.L. Litvak, D.I. Lisov, R. Starr, W. Boynton, A. Behar, L. DeFlores, F. Fedosov, D. Golovin, C. Hardgrove, K. Harshman, I. Jun, A.S. Kozyrev, R.O. Kuzmin, A. Malakhov, R. Milliken, M. Mischna, J. Moersch, M.I. Mokrousov, S. Nikiforov, V.N. Shvetsov, C. Tate, V.I. Tret'Yakov, A. Vostrukhin, Data processing of the active neutron experiment DAN for a martian regolith investigation, Nucl. Instrum. Methods Phys. Res. A 789 (2015) 114–127.

[46] L. Heffern, C. Hardgrove, E. Johnson, A. Parsons, T. Prettyman, A. Jain, H. Barnaby, J. Christian, C. Tate, G. Stoddard, A. Martin, J. Moersch, Active nuclear investigations of planetary surfaces with SINGR (SIngle-Scintillator Neutron and Gamma Ray Spectrometer), in: Lunar and Planetary Science Conference, The Woodlands, TX, 2018, p. 2249.

[47] S. Vogel, R. Frank, G. Stoddard, J.F. Christian, E.B. Johnson, C. Hardgrove, R. Starr, S. West, Development of the LunaH-Map miniature neutron spectrometer, in: M. Fiederle, A. Burger, L. Franks, R.B. James, S.A. Payne (Eds.), Hard X-Ray, Gamma-Ray, and Neutron Detector Physics XIX, 10392, SPIE-Intl Soc Optical Eng, 2017, p. 16.

[48] D. Coupland, L. Stonehill, K. Mesick, J. Dunn, The SENSER CLYC experiment, in: 2016 IEEE Nuclear Science Symposium, Medical Imaging Conference and Room-Temperature Semiconductor Detector Workshop, NSS/MIC/RTSD, 2016, pp. 1–4.

[49] P.R. Menge, D. Richaud, Behavior of Cs2LiYCl6:Ce scintillator up to 175C, in: IEEE Nuclear Science Symposium Conference Record, Institute of Electrical and Electronics Engineers Inc, 2011, pp. 1598–1601.

[50] P.N. Peplowski, M. Burks, J.O. Goldsten, S. Fix, L.E. Heffern, D.J. Lawrence, Z.W. Yokley, Radiation damage and annealing of three coaxial n-type germanium detectors: Preparation for spaceflight missions to asteroid 16 Psyche and Mars' moon Phobos, Nucl. Instrum. Methods Phys. Res. A 942 (2019) 162409.

[51] T. Gabriel, C. Hardgrove, Analysis of Active Neutron Data for In-Situ Planetary Bulk Geochemistry, in: Lunar and Planetary Science Conference, 2020, p. 2888.

[52] M. Watts, K. Mesick, K. Bartlett, D.S. Coupland, Thermal characterization of Tl_2LiYCl_6:Ce (TLYC), IEEE Trans. Nucl. Sci. 67 (3) (2019) 525–533.